RSC Sustainability

ROYAL SOCIETY OF CHEMISTRY

PAPER

View Article Online
View Journal | View Issue

Cite this: *RSC Sustainability*, 2025, **3**, 572

Electrochemical upgrade of 5-hydroxymethylfurfural by C–N coupling over etched $CuAu_3$@CuPd nanocubes†

Zi-Yuan Li, Jiang Shao, Yi-Fei Zhang, Xiao-Yu Guo, De-Jiu Wang, Hao Dong and Ya-Wen Zhang *

5-Hydroxymethylfurfural (HMF), as a direct product of cellulose degradation, is an important biomass-based platform compound. The reductive amination of HMF is of significant industrial value among the upgrading reactions of HMF, which produces 5-hydroxymethylfurfurylamine (5-(aminomethyl)-2-furanmethanol, HMFA), an important intermediate of pharmaceutical and polymer materials. This work presents a facile one-pot synthesis of $CuAu_3$@CuPd nanocubes, which demonstrate exceptional activity and selectivity in the electrochemical co-reduction of HMF and NO_3^- to yield HMFA. Furthermore, an optimal faradaic efficiency of over 75% was achieved by etching the nanoalloy material with a moderate concentration of $NOBF_4$. The etching process exposed deeper CuPd active sites with a lattice distortion affected by the $CuAu_3$ core, thereby promoting the catalytic activity. Catalytic mechanism studies indicate that the C–N coupling reaction pathway involves the *in situ* generation and capture of the $^*NH_2OH$ intermediate. This work has paved a promising pathway for synthesizing high-value products from abundant biomass precursors utilizing the inorganic pollutant NO_3^- as a nitrogen source under ambient electrochemical conditions through the electrochemical co-reduction of HMF and NO_3^-.

Received 11th November 2024
Accepted 19th December 2024

DOI: 10.1039/d4su00700j

rsc.li/rscsus

Sustainability spotlight

The global shift towards sustainable energy and materials is crucial for addressing the depletion of non-renewable resources and environmental degradation. Biomass, as the only renewable organic carbon resource, offers a promising alternative. 5-Hydroxymethylfurfural (HMF), derived from the dehydration of hexose sugars, is a crucial biomass-based platform molecule with significant potential for producing high-value chemicals. This work addresses these issues by developing a novel electrochemical method for the reductive amination of HMF to produce 5-hydroxymethylfurfurylamine (HMFA), an important intermediate in pharmaceuticals and polymers. This method not only uses renewable energy sources, but also utilizes inorganic pollutant nitrate as a nitrogen source, significantly reducing the environmental impact and enhancing the value of biomass. The sustainable advancement of this work aligns with the United Nations Sustainable Development Goals (SDGs) 9 (industry, innovation, and infrastructure) and 12 (responsible consumption and production).

Introduction

With the increasing prominence of global energy and environmental issues, finding alternatives to non-renewable fossil resources such as coal, oil, and natural gas has become a major focus for both academia and industry.[1] Biomass and its derived platform molecules have gained significant attention as the only renewable organic carbon resource because of their safety, cleanliness, and renewability.[2] However, the utilization of biomass often faces challenges, such as low raw material purity, incomplete conversion, numerous by-products, low utilization efficiency and low added value of products, driving researchers to further optimize methods for developing and utilizing biomass resources.[3]

5-Hydroxymethylfurfural (HMF) has been recognized as an important biomass-based platform molecule.[4] HMF is primarily derived from the dehydration of hexose sugars like glucose and fructose obtained from cellulose degradation.[5–7] The HMF molecule structure contains a furan ring, an aldehyde group, and a hydroxymethyl group, which confer relatively high organic reactivity, facilitating subsequent chemical development and upgrading to produce a range of high-value target products, including pharmaceutical molecules and novel polymer materials.[8] Among the upgrading reactions of HMF, its reductive amination holds significant production value.[9] The product, 5-hydroxymethylfurfurylamine (5-(aminomethyl)-2-furanmethanol, HMFA), is an important intermediate in

Beijing National Laboratory for Molecular Sciences (BNLMS), State Key Laboratory of Rare Earth Materials Chemistry and Applications, PKU-HKU Joint Laboratory in Rare Earth Materials and Bioinorganic Chemistry, College of Chemistry and Molecular Engineering, Peking University, Beijing 100871, China. E-mail: ywzhang@pku.edu.cn

† Electronic supplementary information (ESI) available: Experimental section, additional XRD data, XPS spectra, TEM images and details of additional electrochemical tests (pdf). See DOI: https://doi.org/10.1039/d4su00700j

pharmaceuticals and polymer materials.[9,10,12] The amino functional group in the HMFA molecule provides it with more universal reactivity as a versatile molecular building block. Currently, there are two main methods of producing HMFA from HMF. One of them is the homogeneous method, which is commonly used in industrial production. However, this method involves the use of concentrated acid and therefore has its limitations, such as high corrosiveness to reaction vessels, high energy consumption and low yield.[10] The other method is heterogeneous thermal catalysis, which involves using corrosive NH_3 and flammable H_2 in a reactor in the presence of a heterogeneous catalyst at high temperature and pressure.[10–12] This method requires harsh operating conditions, leading to safety concerns, high energy consumption and challenges in catalyst separation and numerous side reactions. Therefore, it is urgent to find alternative pathways for the environmentally friendly synthesis of HMFA.

Research on electrochemical upgrading of HMF has been reported in recent years, mostly focusing on the anodic electrochemical oxidation of HMF to produce 2,5-furandicarboxylic acid.[13–15] Reports on the electrochemical reductive amination of HMF are still scarce, and electrochemical synthesis of HMFA from HMF has not been reported to date. In 2016, Roylance *et al.* first reported the electrochemical reductive amination of HMF.[16] They proposed a reaction pathway, where a primary amine captures the aldehyde group of HMF to form an imine, which is then reduced to a secondary amine on the cathode of an aqueous electrolytic reactor, using water as the proton source. In this work, methylamine was used as the nitrogen source, and the electrochemical reductive amination of HMF was carried out over an Ag dendritic electrode with a larger specific surface area, achieving >99% faradaic efficiency and selectivity at a potential of −1.1 V *vs.* RHE. In 2022, Zhang *et al.* published two consecutive studies investigating the electrochemical reductive amination of HMF using a TiS_2 material with sulfur vacancies and a Ti-MOF as an electrocatalyst, respectively, with ethanolamine as the nitrogen source.[17,18] All the aforementioned studies used organic amine molecules as the nitrogen sources, which brought about additional raw material costs and limited the functional group structure of the product. On the other hand, the electrocatalytic reductive amination (ERA) of carbonyl substrates (ketones or aldehydes) with inorganic ammonia or nitrate as a nitrogen source has attracted researchers' attention.[19,20] Therefore, a combination of biomass-derived HMF upgrading and waste NO_3^- usage was explored in this work.

Herein, this work reports a novel electrochemical method for the reductive amination of HMF by coupling the electrochemical reduction products of NO_3^- with HMF (Fig. 1). By designing and optimizing a novel $CuAu_3$@CuPd nanoalloy catalyst, this work achieved efficient and ambient electrosynthesis of HMFA in aqueous solution, with a faradaic efficiency of up to 75.52% and a yield of 3582.82 mg g_{cat}^{-1} h^{-1}. After over 14 hours of continuous stability testing, the catalyst activity showed only a slight decrease. A series of characterization experiments were conducted to investigate the structure and activity sites of the catalyst. *In situ* attenuated total reflection surface enhanced infrared absorption spectroscopy (ATR-SEIRAS) and differential electrochemical mass spectrometry

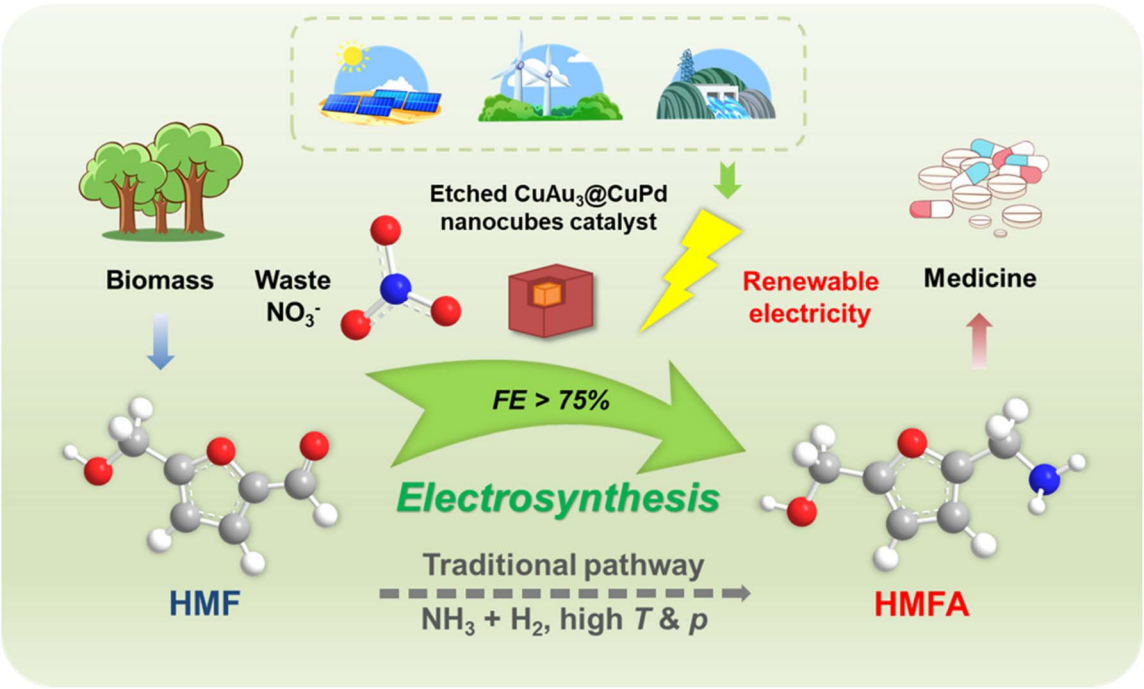

Fig. 1 Schematic diagram of direct electrosynthesis of HMFA from biomass-derived HMF and waste nitrate driven by renewable energy sources under ambient conditions.

(DEMS) experiments were conducted to reveal the reaction mechanism.

Results and discussion

Material synthesis and characterization

A core–shell cubic structure Cu–Pd–Au alloy nanocrystal (denoted as CPA) was firstly synthesized in one pot under an Ar atmosphere, using oleylamine as the solvent and reducing agent and trioctylphosphine (TOP) as the morphology control agent, with an optimized feed ratio, temperature, and reaction time (Fig. 2a).[21,22] During the synthesis, as the reaction temperature gradually increased from room temperature to 80–120 °C, the color of the reaction mixture changed from blue-green to yellow and then to colorless. This color change corresponds to the reduction of Cu(II) and Au(III) with higher reduction potentials to Cu(I) and Au(I), forming complexes with oleylamine and TOP molecules, which become precursors for seed growth.[23] As the temperature further increased to 240–280 °C, the reaction solution underwent explosive nucleation, generating a large amount of reddish-brown precipitate. At this stage, Cu(I) and Au(I) were reduced to Cu(0) and Au(0) and formed seeds, which further grew epitaxially to form nanocrystal cores with cubic morphology. After the Au precursor was exhausted, Pd and the remaining Cu continued to grow epitaxially on the surface of the Cu–Au core due to lattice match, forming a shell rich in Cu and Pd elements.[24] In order to remove adsorbed residuals and create more surface defect sites, the synthesized CPA was treated with different concentrations of the Lewis acid reagent $NOBF_4$, resulting in moderately etched CPA-5 and deeply etched CPA-10 samples.[25,26]

The morphology and microstructure of the synthesized catalysts were analyzed using high-resolution transmission electron microscopy (HRTEM) and powder X-ray diffraction (PXRD). In the HRTEM and STEM images, there was a significant difference between the shells and cores of individual nanoparticles, indicating the formation of a core–shell nanostructure. CPA nanoparticles (Fig. S1†) had a complete cubic morphology, while the shell of moderately etched CPA-5 (Fig. 2b and c) had many holes, and the shell of deeply etched CPA-10

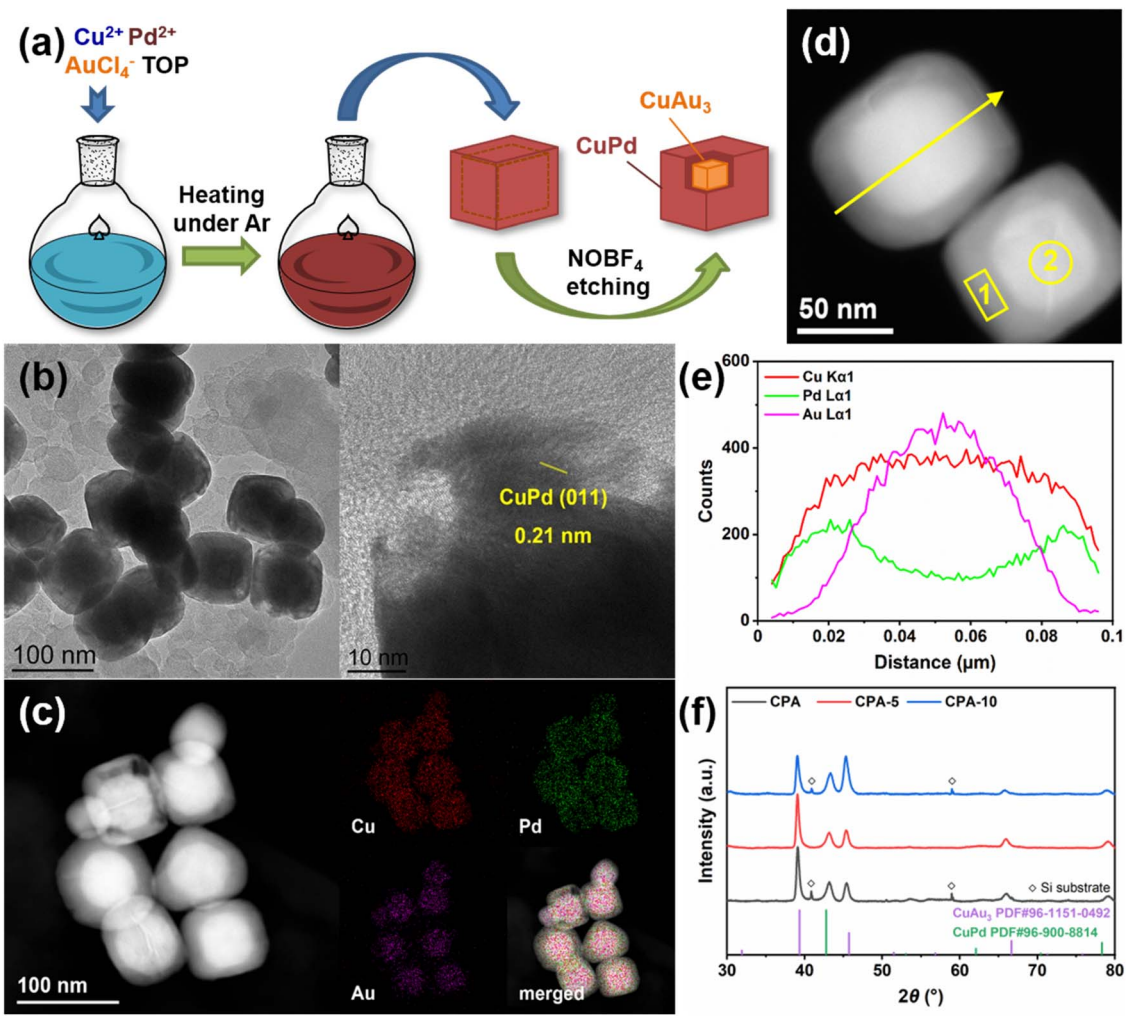

Fig. 2 Synthesis and structural characterization of the catalysts. (a) Schematic illustration of the synthetic procedure of CPA, CPA-5 and CPA-10. (b) HRTEM images of CPA-5. (c) EDS mappings of Cu, Pd and Au for CPA-5. (d) STEM image and (e) EDS line scan result of CPA. (f) PXRD spectra of CPA, CPA-5 and CPA-10.

samples almost completely disappeared, exposing the inner core (Fig. S2†). In the XRD patterns of the CPA sample (Fig. 2f), there were strong diffraction peaks at $2\theta = 39.1°$, 43.2°, and 45.4°. The diffraction peaks located at 39.1° and 45.4° correspond to the peaks of bcc $CuAu_3$ (111) and (002) crystal planes, respectively, with a shift of 0.2° and 0.3°to a smaller angle, respectively. The diffraction peak at 43.2° corresponds to the bcc CuPd (011) peak, shifted by 0.5° to a larger angle. The shifts of diffraction peaks indicated that the Cu–Au core and Cu–Pd shell of the core–shell structure may affect the mutual lattices, causing lattice distortions in both layers.[21,22] In the XRD patterns of CPA-5 and CPA-10 samples (Fig. 2f), larger shifts of diffraction peaks were observed, indicating that the inner layer with larger lattice distortion was exposed due to the etching of $NOBF_4$. This crystal lattice distortion can cause surface strain and thus lead to a geometric effect and have a possible influence on the catalytic performances of the materials.[21] Moreover, the intensity of the peak at 45.3° of CPA-10 increased, showing a larger exposure of the (001) surface of the $CuAu_3$ core. In the HRTEM images, the lattice fringes with a spacing of 0.21 nm were measured in both CPA (Fig. S1a†) and moderately etched CPA-5 samples (Fig. 2b), matching the bcc CuPd (011) crystal plane spacing. Additionally, in the deeply etched CPA-10 samples (Fig. S2a†), lattice fringes with spacings of 0.15 nm and 0.22 nm were measured in the edge and center regions, respectively, matching the bcc CuPd (002) and fcc $CuAu_3$ (002) crystal plane spacings.

The elemental composition and distribution of the synthesized nanoalloys were studied using scanning tunneling electron microscopy (STEM) and X-ray energy dispersive spectroscopy (EDS). The EDS mapping (Fig. S1b†) and line scan results (Fig. 2d and e) of CPA further confirmed that Pd was mainly distributed in the shell, Au was mainly distributed in the core region, and Cu was relatively evenly distributed throughout the nanoparticles. Furthermore, the EDS results of multiple CPA nanoparticles (Table 1) showed an elemental ratio of approximately $Cu : Pd : Au = 4 : 3 : 3$ (atomic ratio), which was further confirmed by inductively coupled plasma-optical emission spectroscopy (ICP-OES, Table 1, row 2). To make it clear, two regions of the shell (1) and core (2) on a single CPA nanoparticle were selected for EDS analysis of their elemental composition (Fig. 2d and Table 1). It was found that the shell had similar Cu and Pd content with little Au, while the core had decreased Pd content, though it was still present, due to the shell covering all surfaces of the cube. The Cu content minus the Pd content was close to 1/3 of the Au content.

Table 1 EDS results of Cu, Pd and Au for CPA, CPA-5 and CPA-10, and (*) ICP-OES results of Cu, Pd and Au for CPA

Sample	Cu (atom%)	Pd (atom%)	Au (atom%)
CPA	40.37	32.75	26.88
CPA*	38.28	29.60	32.13
CPA-5	40.37	35.06	24.57
CPA-10	28.51	9.63	61.87
CPA: Area 1	45.61	47.17	7.22
CPA: Area 2	40.51	18.26	41.23

X-ray photoelectron spectroscopy (XPS) was applied to investigate the surface elemental valence states of CPA, CPA-5 and CPA-10 samples (Fig. S3†). The peaks of Cu(0), Pd(0) and Au(0) were observed in all of the spectra, confirming that the Cu, Pd and Au elements existed in their alloy forms in CPA, CPA-5 and CPA-10 catalysts. Besides, the binding energy of Cu $2p_{3/2}$ in CPA-10 slightly increased, indicating electron transfer from Cu to Au and further proving the presence of the $CuAu_3$ intermetallic compound in the core.[21,22] In summary, the composition and structure of the synthesized nanoparticles can be denoted as $CuAu_3$@CuPd nanocubes.

Catalytic performance and electrochemical characterization

The synthesized catalyst was applied to the electrocatalytic HMF-NO_3^- co-reduction reaction under optimized reaction conditions in an H-type electrolytic cell. The products of this reaction were qualitatively and quantitatively analyzed using gas chromatography (GC) and ^{1}H nuclear magnetic resonance (^{1}H-NMR) (Fig. 3). In the ^{1}H-NMR spectrum (Fig. 3a), HMFA exhibited characteristic double peaks at 6.2 and 6.3 ppm, corresponding to the two hydrogen atoms on the furan ring of the HMFA molecule. The corresponding peak at 6.2 ppm was observed in the electrolyte after the reaction, confirming the formation of the HMFA product, and was used to quantify the product. In the GC spectrum (Fig. 3b), the retention times for HMF and HMFA were 3.5 minutes and 4.55 minutes, respectively. Both peaks were present in the GC spectrum of the electrolyzed solution, further confirming the presence of HMFA. The standard curve of HMFA was obtained by ^{1}H-NMR (Fig. S3†) in order to quantitate HMFA in the production. The main competing reactions involve the individual electroreduction of the C-source (HMF) and N-source (NO_3^-), producing 2,5-furandimethanol and NH_4^+, respectively. During all the experiments, almost no bubble generation was observed, indicating that the hydrogen evolution reaction (HER) had a minimal impact on the overall reaction system.

In the catalytic tests of the catalysts and control samples (commercial Cu nanoparticles (NPs), Au NPs and Pd/C catalyst) (Fig. 4a), the moderately etched CPA-5 sample showed superior FE and space-time yield compared to the original CPA and the deeply etched CPA-10 samples, corresponding to the formation and destruction of active sites, following the Sabatier principle. The FE reached 75.52%, and the yield was 3582.82 mg g_{cat}^{-1} h^{-1} at a current density of 20 mA cm^{-2}, the highest among all the explored electrocatalysts, with a conversion rate of 12.52% (Table S2†). The space-time yield of CPA-5 is higher than those of previously reported HMF amination catalysts running under solvothermal conditions, due to the low catalyst usage of electrocatalysis. Moreover, the electrocatalysis reaction pathway also avoids the use of high pressure NH_3 and H_2 gas, as well as organic solvents or acids, thus showing superior advantages in environmental protection, as well as green and sustainable chemistry. Long-term stability tests of the CPA-5 catalyst (Fig. 4b) showed that the cathodic reductive potential remained generally stable, with only a slight decline in FE during and after a 14.25 h continuous test. The HRTEM image and EDS mapping

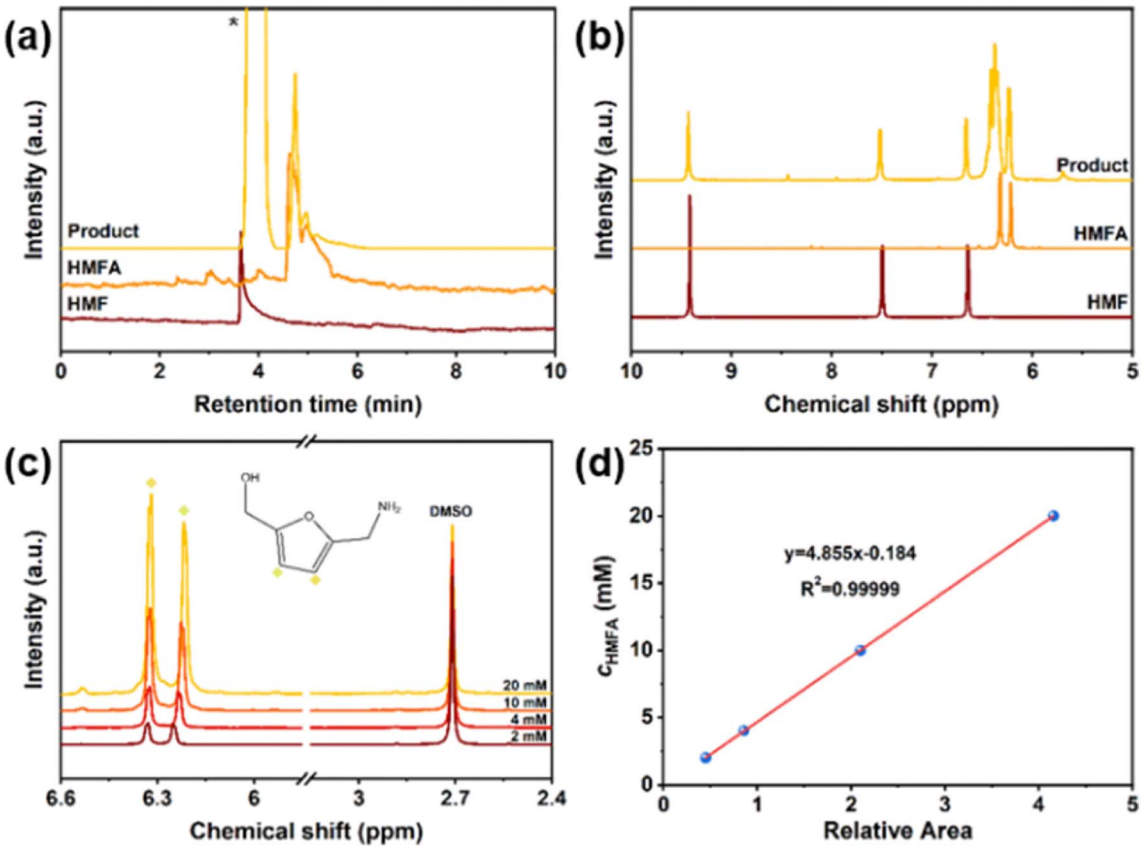

Fig. 3 HMFA Product analysis. (a) GC (*: solvent peak) and (b) ^{1}H-NMR results of the electrolysis product. (c) ^{1}H-NMR standard curves of HMFA. (d) Linear fitting result of the ^{1}H-NMR standard curves of HMFA.

of CPA-5 after electrocatalysis (Fig. S4 and Table S1†) showed that the catalyst experienced no obvious change in morphologies and element distribution, further proving the outstanding stability. The CPA-5 catalyst after the reaction was characterized using HRTEM, EDS, PXRD and XPS measurements (Fig. S4 and S5†), and the results showed that the morphology, composition,

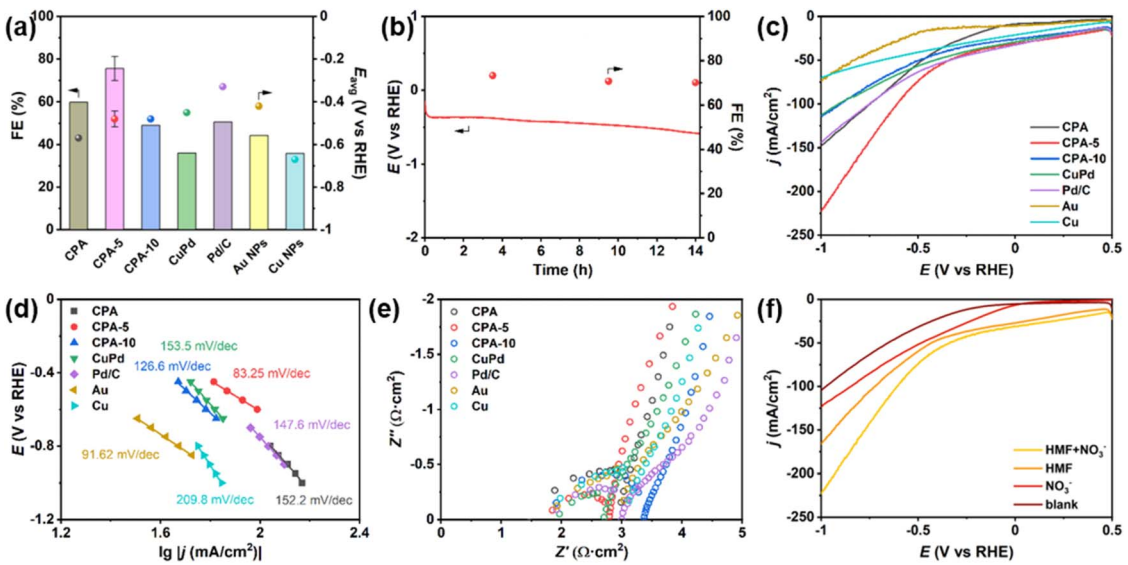

Fig. 4 Catalytic performance and electrochemical characterization of the catalysts. (a) Faradaic efficiencies and average potentials of CPA, CPA-5, CPA-10 and control samples. (b) Long-term stability test of CPA-5. (c) LSV, (d) Tafel slopes and (e) EIS results of CPA, CPA-5, CPA-10 and control samples. (f) LSV tests of CPA-5 in different electrolytes.

structure, and element valence states remained consistent with those before the reaction, proving that the CPA-5 catalyst did not undergo significant changes before and after the electrocatalytic reaction, further confirming its outstanding stability.

To explain the origin of the excellent catalytic activity of CPA-5, a series of comparative experiments were designed and performed. CuPd nanocubes (Fig. S6†) were synthesized *via* a previously reported procedure,[27] and tested under the same conditions for their catalytic performance. The results showed that the FE of the CuPd nanocubes decreased compared to commercial Cu NPs, Au NPs and Pd/C catalysts, indicating that the intrinsic activity of the pure CuPd alloy was relatively low and could not enhance the catalytic performance compared to individual metal nanoparticles. However, the situation changed when $CuAu_3$ cores were introduced. The FE of the unetched CPA was superior to that of the CuPd nanocubes and individual metal catalysts, suggesting that the introduction of the Au-containing core and the formation of the core–shell structure helped to enhance the catalytic activity of the CuPd nanoscale alloy. Furthermore, due to appropriate etching, the deeper CuPd sites in moderately etched CPA-5 were fully exposed, which were closer to the $CuAu_3$ core and thus experienced greater lattice distortion, thereby exhibiting superior catalytic activity. On the other hand, CPA-10 experienced a significant loss of the CuPd shell layer due to excessive etching, resulting in a decrease in the number of active sites and a consequent drop in FE. In summary, based on the comparative experiments on catalytic performance and characterization, it can be inferred that the CuPd nanoalloy phase with lattice distortion serves as the active site for the catalytic reaction.

A series of electrochemical characterization studies were performed to investigate the activity differences between the CPA-5 sample and other control samples (Fig. 4c–f). Linear sweep voltammetry (LSV) data (Fig. 4c) showed that CPA-5 had the highest current density at the same reduction potential. The Tafel slopes (Fig. 4d) were all close to the theoretical value of 118 mV dec^{-1}, indicating that the first electron transfer step of NO_3^- reduction was the rate determining step.[19,28] The Tafel slope of CPA-5 was 83.25 mV dec^{-1}, the lowest among all tested catalysts and controls, indicating the highest charge transfer rate and kinetically favorable conditions for the electrocatalytic reaction. Electrochemical impedance spectroscopy (EIS) tests (Fig. 4e) showed that CPA-5 had the smallest semicircle diameter in the Nyquist plot, representing the lowest charge transfer resistance. Additionally, cyclic voltammetry (CV) tests at different scan rates (20–100 mV s^{-1}) (Fig. S7†) showed that moderately etched CPA-5 had the largest double-layer capacitance (C_{dl}) (Fig. S8 and Table S2†) among all the metal nanoparticle catalysts, while the double-layer capacitance of deeply etched CPA-10 decreased, possibly because of the destruction of the "holey" shell structure. Thus, it can be indicated that moderate etching enhances the specific surface area of alloy nanocrystals, creating more active sites, consistent with previous assumptions. In addition, LSV tests were conducted on CPA-5 in electrolytes containing different substrates (Fig. 4f). The reductive current density in the electrolyte containing both HMF and NO_3^- is higher than those with one or no substrate, confirming the occurrence of the co-reduction reaction of HMF and NO_3^-.

Reaction mechanism study

To investigate the reaction mechanism of the electrocatalytic HMF-NO_3^- co-reduction reaction, a series of control experiments with different substrates were designed. NO_2^-, NH_2OH, N_2 and NH_4^+ with equal concentrations were used respectively as nitrogen sources for the co-reduction reaction with HMF (Table 2). The results showed that HMFA products were formed with the catalysis of CPA-5 when NO_2^- and NH_2OH were used as nitrogen sources, but not with N_2 or NH_4^+. This suggests that the reaction mechanism might be as follows: NO_3^- is first adsorbed onto the catalyst surface and reduced to $^*NO_2$, which then undergoes a series of proton and electron transfer processes to form the adsorbed hydroxylamine intermediate $^*NH_2OH$. This active intermediate nucleophilically attacks the aldehyde group in HMF and thus captures the HMF molecule by the oximation reaction, and the resulting oxime is further reduced to an amine, yielding the final product HMFA.

According to relevant research reports, the rate-determining step of the nitrate-involved co-reduction C–N coupling reaction is primarily the reduction of nitrate to nitrite.[28,29] To demonstrate the effect of lattice distortion on the rate-determining step, we tested the LSV performance of catalysts with different degrees of lattice distortion in the CuPd surface layer (CPA-5, CPA, and CuPd NCs) under nitrate reduction conditions (Fig. S9†). The main sample CPA-5 exhibited a higher reduction current density (Fig. S9a†) and a lower Tafel slope (Fig. S9b†), further confirming that CuPd with lattice distortion serves as the active site for the catalytic reaction.

To verify the proposed reaction mechanism, differential electrochemical mass spectrometry (DEMS) and *in situ* attenuated total reflection surface enhanced infrared absorption spectroscopy (ATR-SEIRAS) were used to further characterize the intermediates under reaction conditions (Fig. 5). In the DEMS test (Fig. 5a), pulsed reduction potentials were applied to NO_3^- solution and (NO_3^- + HMF) solution, respectively, while a molecular pump applied a negative pressure on the back of the gas diffusion electrode to draw the gas-phase intermediates into the mass spectrometer, recording the signal intensity for different m/z changes over time. It was found that the peak signal intensities for $m/z = 2$ (corresponding to H_2) and 17 (corresponding to NH_3) did not change significantly before and after adding HMF to the NO_3^- reduction system, while the signal intensity for $m/z = 33$ (corresponding to NH_2OH)

Table 2 Results of the control experiments with different substrates

Catalyst	C source	N source	Product
CPA-5	HMF	NO_2^-	√
CPA-5	HMF	NH_2OH	√
CPA-5	HMF	N_2	×
CPA-5	HMF	NH_4^+	×
Carbon paper	HMF	NO_3^-	×

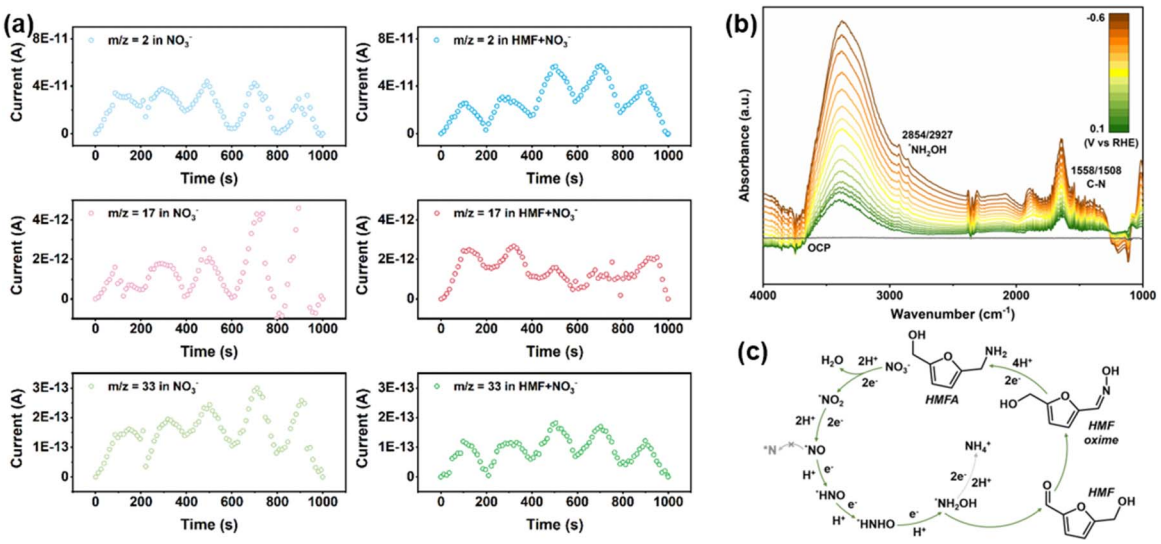

Fig. 5 Reaction mechanism study. (a) DEMS results and (b) *in situ* ATR-SEIRAS spectra of the electrocatalytic HMF-NO_3^- co-reduction reaction. (c) Proposed reaction mechanisms.

significantly decreased in the solution containing HMF and NO_3^- compared to the solution containing only NO_3^- during electroreduction. This indicates that the $^*NH_2OH$ intermediate generated during the cathodic reduction of NO_3^- was captured and consumed by HMF.[19,30]

In situ ATR-SEIRAS spectra (Fig. 5b) were collected by applying increasingly negative reduction potentials to the solution containing HMF and NO_3^-. As the applied potential became more negative, two characteristic absorption peaks appeared at 2854 and 2927 cm^{-1}, corresponding to the characteristic vibrations of the primary amine C–N bond.[30,31] Moreover, vibration peaks of the C–N bond were observed at 1558 and 1508 cm^{-1}, confirming the presence of C–N coupling products.[8] In summary, the proposed reaction pathway for the electrocatalytic HMF-NO_3^- co-reduction reaction can be represented as: $NO_3^- \rightarrow {}^*NO_2 \rightarrow {}^*NO \rightarrow {}^*HNO \rightarrow {}^*HNHO \rightarrow {}^*NH_2OH$ and $^*NH_2OH$ + HMF → HMF oxime → HMFA.

Conclusions

This work reports a facile one-pot synthesis of $CuAu_3$@CuPd nanocubes as an electrocatalyst for the electrocatalytic co-reduction of 5-hydroxymethylfurfural (HMF) and NO_3^-, exhibiting considerable activity and selectivity towards the production of 5-hydroxymethylfurfuryl amine ((5-(amino-methyl)furan-2-yl)methanol, HMFA), which is an important medical intermediate. Moreover, an optimized faradaic efficiency of 75.52% and a yield of 3582.82 mg g_{cat}^{-1} h^{-1} was achieved by etching the nanoalloy material with a moderate concentration of $NOBF_4$. The moderate etching exposed deeper CuPd active sites with a lattice distortion affected by the $CuAu_3$ core, thereby promoting the catalytic activity. Electrochemical characterization revealed that a moderately etched catalyst (denoted as CPA-5) shows larger double-layer capacitance (C_{dl}) and faster electron transfer, resulting in accelerated reaction kinetics. The results of *in situ* IR spectroscopy and differential electrochemical mass spectrometry (DEMS) reveal that the C–N coupling reaction pathway involves the *in situ* generation and capture of the NH_2OH intermediate. In an alkaline environment, nitrate reduction follows the mechanism: $NO_3^- \rightarrow {}^*NO_2 \rightarrow {}^*NO \rightarrow {}^*HNO \rightarrow {}^*HNHO \rightarrow {}^*NH_2OH$ and $^*NH_2OH$ + HMF → HMF oxime → HMFA. In summary, this work has developed a novel pathway for synthesizing high-value-added products under mild electrochemical conditions by the electrochemical co-reduction of 5-hydroxymethylfurfural (HMF) and NO_3^-, utilizing inexpensive biomass precursors and the inorganic pollutant NO_3^- as a nitrogen source.

Data availability

The data that support the findings of this article are openly available in the ESI.†

Author contributions

Ya-Wen Zhang conceived the idea and directed the project. Zi-Yuan Li designed the experiments and carried out the materials synthesis and characterization and electrochemical tests. Jiang Shao contributed to the result discussion and mechanism analysis and helped in the *in situ* ATR-SEIRAS test and the drawing of the schematic diagram. Yi-Fei Zhang contributed to the ^{1}H-NMR standard curves. Xiao-Yu Guo helped in the ICP-OES test. De-Jiu Wang helped in the XPS test. Zi-Yuan Li wrote the paper. Ya-Wen Zhang and Hao Dong revised the manuscript. All authors discussed the results and commented on the manuscript.

Conflicts of interest

The authors declare no conflicts of interest.

Acknowledgements

This work was supported by the National Key R&D Program of China (no. 2023YFA1506800), the National Natural Science Foundation of China (no. 22293042), and the Beijing National Laboratory for Molecular Sciences (BNLMSCXXM-202104). We greatly acknowledge Prof. Jie Zheng and Shao-lei Yang (PhD candidate) from Peking University for their help with the *in situ* ATR-SEIRAS and DEMS tests. We sincerely thank the NMR facility at the National Center for Protein Sciences at Peking University for assistance with ^{1}H-NMR.

References

1 Y. Gao, L. Ge, H. Xu, K. Davey, Y. Zheng and S. Z. Qiao, *ACS Catal.*, 2023, 11204–11231.
2 K. Wang, Z. Li, Z. Guo, J. Huang, T. Liu, M. Zhou, J. Hu and H. Li, *Green Chem.*, 2024, **26**, 2454–2475.
3 J. Slak, B. Pomeroy, A. Kostyniuk, M. Grilc and B. Likozar, *Chem. Eng. J.*, 2022, **429**, 132325.
4 I. K. M. Yu and D. C. W. Tsang, *Bioresour. Technol.*, 2017, **238**, 716–732.
5 I. J. Kuo, N. Suzuki, Y. Yamauchi and K. C. W. Wu, *RSC Adv.*, 2013, **3**, 2028–2034.
6 P. Körner, D. Jung and A. Kruse, *Green Chem.*, 2018, **20**, 2231–2241.
7 Y. Su, H. M. Brown, X. Huang, X. D. Zhou, J. E. Amonette and Z. C. Zhang, *Appl. Catal., A*, 2009, **361**, 117–122.
8 K. Gupta, R. K. Rai and S. K. Singh, *ChemCatChem*, 2018, **10**, 2326–2349.
9 C. C. Truong, D. K. Mishra and Y. W. Suh, *ChemSusChem*, 2023, **16**, 1–14.
10 W. Chen, Y. Sun, J. Du, Z. Si, X. Tang, X. Zeng, L. Lin, S. Liu and T. Lei, *J. Chem. Technol. Biotechnol.*, 2018, **93**, 3028–3034.
11 Z. Wei, Y. Cheng, K. Zhou, Y. Zeng, E. Yao, Q. Li, Y. Liu and Y. Sun, *ChemSusChem*, 2021, **14**, 2308–2312.
12 D. Ruiz, K. Morales, P. Mäki-Arvela, R. J. Chimentão and D. Y. Murzin, *Chempluschem*, 2024, e202400453.
13 Y. Lu, T. Liu, Y. C. Huang, L. Zhou, Y. Li, W. Chen, L. Yang, B. Zhou, Y. Wu, Z. Kong, Z. Huang, Y. Li, C. L. Dong, S. Wang and Y. Zou, *ACS Catal.*, 2022, **12**, 4242–4251.
14 S. Li, S. Wang, Y. Wang, J. He, K. Li, Y. Xu, M. Wang, S. Zhao, X. Li, X. Zhong and J. Wang, *Adv. Funct. Mater.*, 2023, **33**, 1–10.
15 C. Liu, X. R. Shi, K. Yue, P. Wang, K. Zhan, X. Wang, B. Y. Xia and Y. Yan, *Adv. Mater.*, 2023, **35**, 1–9.
16 J. J. Roylance and K. S. Choi, *Green Chem.*, 2016, **18**, 5412–5417.
17 M. Zhang, S. Xu, M. Boubeche, D. Decarolis, Y. Huang, B. Liu, E. K. Gibson, X. Li, Y. Wang, H. Luo, C. R. A. Catlow and K. Yan, *Green Chem.*, 2022, **24**, 9570–9578.
18 M. Zhang, D. Hu, Y. Chen, Y. Jin, B. Liu, C. H. Lam and K. Yan, *Ind. Eng. Chem. Res.*, 2022, **61**, 1912–1919.
19 Y. F. Xiao, C. W. Lim, J. Q. Chang, Q. X. Yuan, L. Wang and N. Yan, *Green Chem.*, 2023, **25**, 3117–3126.
20 J. Shao, Y. F. Zhang, S. Z. Xue, Z. Y. Li, X. Li, B. Liang, T. Z. Li, H. Dong and Y. W. Zhang, *Inorg. Chem. Front.*, 2024, **5**, 5286–5298.
21 L. Luo, C. Fu, Y. Guo, X. Cai, X. Luo, Z. Tan, R. Xue, X. Cheng, S. Shen and J. Zhang, *ACS Nano*, 2023, **17**, 2992–3006.
22 C. Hu, X. Chen, J. Low, Y. W. Yang, H. Li, D. Wu, S. Chen, J. Jin, H. Li, H. Ju, C. H. Wang, Z. Lu, R. Long, L. Song and Y. Xiong, *Nat. Commun.*, 2023, **14**, 221.
23 S. Chen, S. V. Jenkins, J. Tao, Y. Zhu and J. Chen, *J. Phys. Chem. C*, 2013, **117**, 8924–8932.
24 A. X. Yin, X. Q. Min, W. Zhu, W. C. Liu, Y. W. Zhang and C. H. Yan, *Chem. – Eur. J.*, 2012, **18**, 777–782.
25 H. J. Yin, J. H. Zhou and Y. W. Zhang, *Inorg. Chem. Front.*, 2019, **6**, 2582–2618.
26 H. J. Yin, Z. P. Zhang, Y. Guo, K. Yuan and Y. W. Zhang, *Mater. Chem. Front.*, 2020, **4**, 1985–1992.
27 Q. Gao, Y. M. Ju, D. An, M. R. Gao, C. H. Cui, J. W. Liu, H. P. Cong and S. H. Yu, *ChemSusChem*, 2013, **6**, 1878–1882.
28 S. Han, H. Li, T. Li, F. Chen, R. Yang, Y. Yu and B. Zhang, *Nat. Catal.*, 2023, **6**, 402–414.
29 G. E. Dima, A. C. A. de Vooys and M. T. M. Koper, *J. Electroanal. Chem.*, 2003, **554–555**, 15–23.
30 W. Chen, Y. Wu, Y. Jiang, G. Yang, Y. Li, L. Xu, M. Yang, B. Wu, Y. Pan, Y. Xu, Q. Liu, C. Chen, F. Peng, S. Wang and Y. Zou, *J. Am. Chem. Soc.*, 2024, **146**, 6294–6306.
31 Y. Yuan, L. Chen, Z. Wan, K. Shi, X. Teng, H. Xu, P. Wu and J. Shi, *Sci. Adv.*, 2024, **10**, 1–13.